

# Approaches to delineate aggregates in intact soil using X-ray imaging

John Koestel<sup>a,b,\*</sup>, Jumpei Fukumasu<sup>a</sup>, Gina Garland<sup>b</sup>, Mats Larsbo<sup>a</sup>, David Nimblad Svensson<sup>a</sup>

<sup>a</sup> Department of Soil and Environment, Swedish University of Agricultural Sciences, Box 7014, 750 07 Uppsala, Sweden

<sup>b</sup> Soil Quality and Soil Use, Agroscope Reckenholz, Reckenholzstrasse 191, 8046 Zürich, Switzerland

## ARTICLE INFO

Handling Editor: Yvan Capowicz

### Keywords:

Soil structure  
Soil aggregate  
X-ray imaging  
Pore network  
Morphology  
Dropshatter test

## ABSTRACT

Soil structure refers to the spatial arrangement of primary soil particles and pores, and is known to influence a variety of soil functions including carbon sequestration and water holding capacity. At present, research in this field is often divided, focusing either on pores where pore networks are investigated in undisturbed soil or on solids where isolated soil aggregates are commonly studied. The choice of approach depends on the needs and traditions in different disciplines of soil science. While there is much debate regarding how well these viewpoints relate to each other, there have been only marginal research efforts undertaken to compare them quantitatively. In this study, we presented and evaluated methods to identify 3-D subunits in X-ray images of eight undisturbed soil samples that we interpreted as macroaggregates, and compared these to results from drop-shatter tests. Here, we exploited the cohesive forces of water that induces shrinkage cracks under drying. Despite promising trends, comparisons between image and drop-shatter test derived aggregate properties remained inconclusive. Nevertheless, our results encourage further investigations on larger sample sets and different observation scales. The here presented and discussed aggregate delineation methods illustrate an approach to harmonize soil structure characterization in terms of both pore-networks and soil aggregation. For example, respective extended approaches may be developed to evaluate the locations of microaggregates within macroaggregates.

## 1. Introduction

The term soil structure, similar to that of soil architecture, refers to the morphology and topology of soil pores and solids (Rabot et al., 2018). It is fundamental to soil functioning as it largely determines the soil hydrologic and aeration properties (Horn et al., 1994). Consequently, it influences soil functions like carbon sequestration, storage of nutrients and retention of contaminants. As soil structure dictates the local distribution of water and redox potentials, it defines habitats for various soil dwelling organisms and guides root growth. The soil biota in turn reshapes and modifies the soil structure, e.g., by introducing new pores through burrowing or aggregating soil particles by mycorrhizal growth or exudation of mucilage.

Soil structure may be investigated from two opposite points of view. The first one focuses on the morphology of the pore network (Rabot et al., 2018). It has been argued that the pore-network perspective is the only relevant one when investigating soil structure, since processes in soil take place in the pores and not in the solids (Young et al., 2001). Sometimes, the term ‘soil architecture’ is used to underline that the soil structure is described in terms of pore morphology and not in terms of

solids. The second point of view describes soil structure by the arrangement of individual mineral and organic primary particles as well as different levels of aggregations (Tisdall and Oades, 1982). According to the Soil Science Society of America (SSSA, 1997), an aggregate is defined as “a group of primary soil particles that cohere to each other more strongly than to other surrounding particles”. There is a vast amount of research published on soil aggregations at the millimetre and sub-millimetre scale, often classified as micro (<250 µm) and macro aggregates (≥250 µm; Six et al., 2004; Totsche et al., 2018). However, also much larger soil aggregations, up to diameters of centimetres and decimetres are referred to as aggregates (e.g. Munkholm et al., 2016; Sexstone et al., 1985). To avoid confusion and following the SSSA, we define a soil aggregate as any aggregation of soil primary particles, regardless of size, that is held together by any kind of cohesive force, be it of biotic origin or not.

It has been well documented that both abiotic and biotic processes are important for the formation of soil aggregates. Fundamental to the abiotic processes are electrostatic forces between silt and especially clay-sized mineral and organic particles, which commonly carry a surface charge. Together with counter ions and the highly polar character of the

\* Corresponding author at: Department of Soil and Environment, Swedish University of Agricultural Sciences, Box 7014, 750 07 Uppsala, Sweden.

E-mail address: [johannes.koestel@agroscope.admin.ch](mailto:johannes.koestel@agroscope.admin.ch) (J. Koestel).

<https://doi.org/10.1016/j.geoderma.2021.115360>

Received 24 November 2020; Received in revised form 7 July 2021; Accepted 18 July 2021

Available online 18 August 2021

0016-7061/© 2021 The Authors. Published by Elsevier B.V. This is an open access article under the CC BY license (<http://creativecommons.org/licenses/by/4.0/>).

**Table 1**

Soil texture (USDA classification), organic carbon content, SOC, total porosity,  $\phi_{tot}$ , and aggregate bulk density,  $\rho_a$ . In cases where the texture fraction do not add up to 1, a respective amount of gravel was present.

Location	Abbreviation	Sand ( $g\ g^{-1}$ )	Silt ( $g\ g^{-1}$ )	Clay ( $g\ g^{-1}$ )	SOC ( $g\ g^{-1}$ )	$\phi_{tot}$ ( $cm^3\ cm^{-3}$ )	$\rho_a$ ( $g\ cm^{-3}$ )
Nåntuna	NA1	0.69	0.11	0.13	0.0128	0.55	1.19
	NA2	0.73	0.11	0.14	0.0089	0.48	1.37
Ultuna/Hammarbyallé	HA1	0.52	0.16	0.31	0.0126	0.47	1.38
	HA2	0.53	0.17	0.3	0.012	0.47	1.38
Krusenberg	KB1	0.37	0.32	0.3	0.0127	0.47	1.39
	KB2	0.37	0.33	0.3	0.0119	0.46	1.42
Ultuna/RAM 1956	RA1	0.21	0.39	0.39	0.0155	0.56	1.14
	RA2	0.22	0.38	0.4	0.0148	0.57	1.13

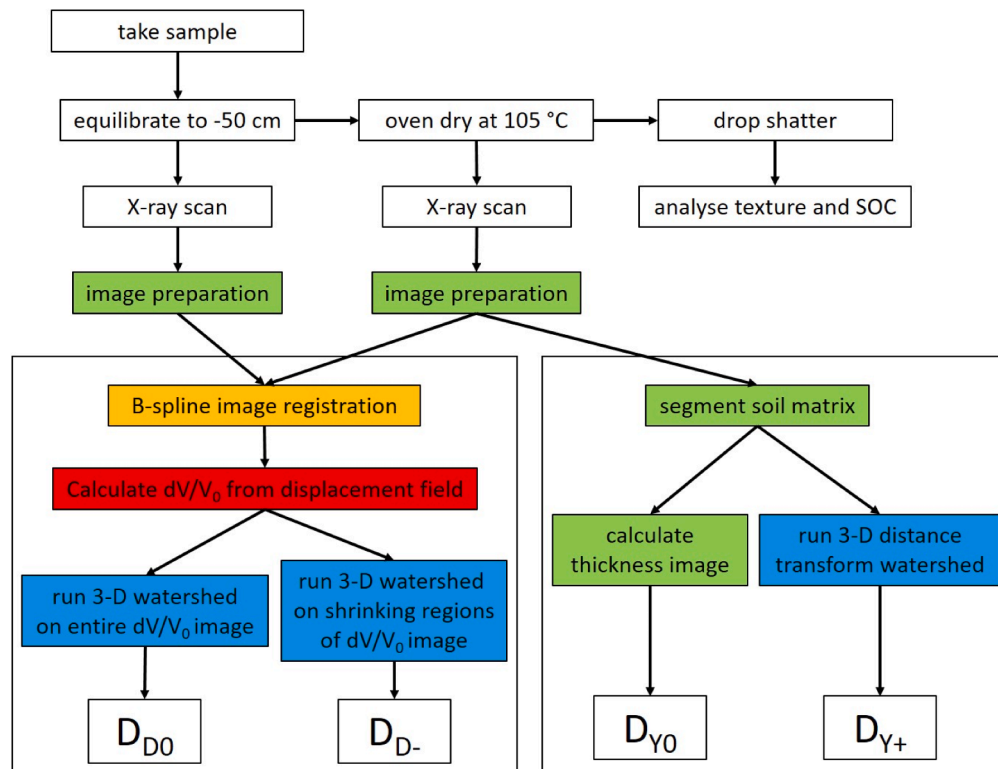


**Fig. 1.** Workflow of the image-based aggregate delineations presented in this study. Colour-coded boxes indicate the software that was used for the respective processing step: “green” – ImageJ/SoilJ, “orange” – elastix, “red” – Matlab, “blue” – ImageJ/MorphoLibJ.

water molecule, which is responsible for a large surface tension and capillarity as well as the formation of hydrogen bonds, they provide the force that acts as a basic binding agent for primary particles (Deneff et al., 2002). In addition, soil aggregates are stabilized by gluing and cementation agents, abiotic in the form of oxides, hydroxides and oxyhydroxides and biotic in form of microbial and root exudations, e.g. polysaccharides (Totsche et al., 2018). In addition, enmeshment of hyphae and roots reinforce the aggregations further (Rillig et al., 2015).

Yet while both viewpoints on soil structure have been adopted from the start of the 20th century (Martin et al., 1955; Stoops, 2009), the number of publications on aggregates clearly outnumbers those on pore networks. This is easily demonstrated by comparing results on SCOPUS using search terms ‘soil’ and ‘aggregate’ (11,835 results) with combinations of ‘soil’ and a keyword addressing the spatial arrangement of pores, namely ‘pore network’, ‘pore structure’ or ‘pore morphology’ (1,406 results if all three are combined by logical OR operators; SCOPUS accessed on 24th November 2020, only considering publications in the field of ‘agricultural and biological sciences’ and ‘environmental sciences’). One reason for this may be the larger efforts required to examine the arrangement of pores in an opaque medium as opposed to

characterizing aggregates created by fragmenting soil (Young et al., 2001). However, a great number of soil properties, e.g. hydraulic and air transport properties, are related to the spatial arrangement of voids and solids in-situ, i.e. the undisturbed pore network (Letey, 1991). Many authors have therefore argued that processes studied in an assortment of displaced aggregates must not be used to infer processes in the undisturbed soil volume from which the aggregates were derived (Baveye, 2020; Kravchenko et al., 2019; Young et al., 2001).

While we fully support this criticism, we also acknowledge that soil aggregation is crucial for soil functioning. Furthermore, although the specific research foci may be quite divergent between studies of soil aggregates and those of pore networks, we hold it as evident that such research is in fact complementary, both possessing merit and contributing to the better understanding of soil structure. Soil pore networks and the arrangement of different solid materials between them express the global topology of soil. When soil aggregates are isolated and investigated, the information of the global topology is lost. In exchange, however, information on the local cohesion between the soil primary particles (i.e. soil structural stability) is gained. Approaches that preserve the information of the original location and orientation of soil

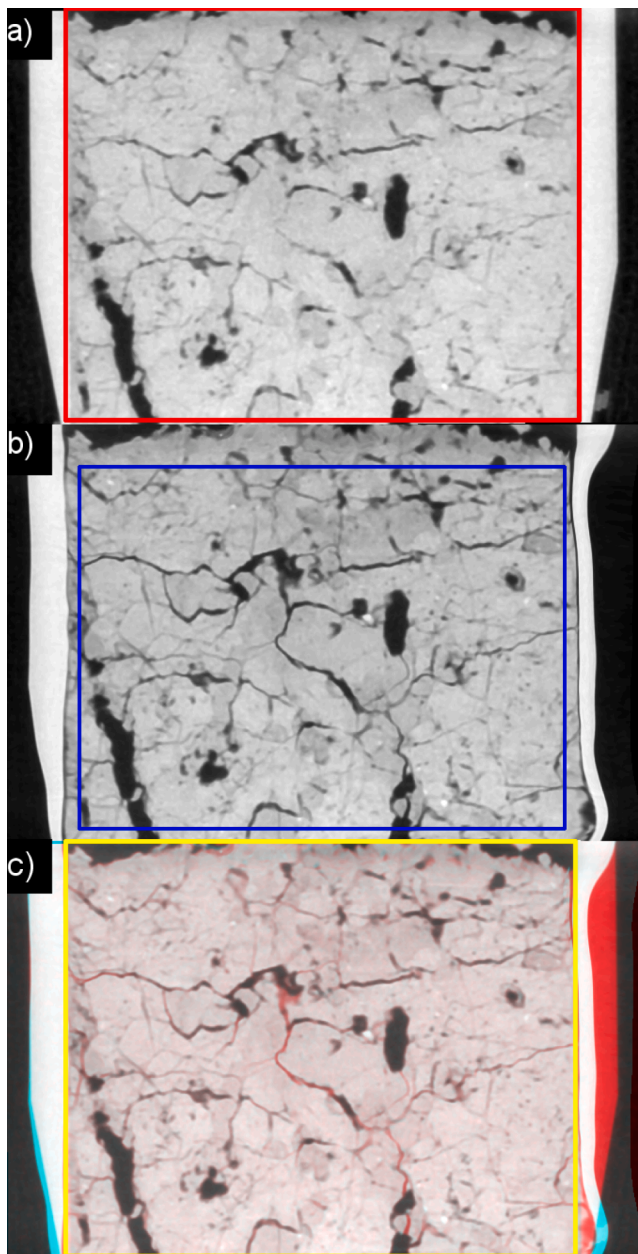


**Fig. 2.** (a) Vertical cross-section through X-ray images of the Krusenberg 1 sample at a tension of 50 cm; (b) the same vertical cross-section of the same sample at the oven-dry state after the B-spline registration; (c) an overlay image of (a) and (b) in which yellow colours indicate a successful match of soil structures. Pairs of red and green colours of similar shape indicate an unsuccessful match of structures, green colours a decrease of local density between (a) and (b). The red (a) and white (c) frames indicate the area that was considered for the registration and the blue frame (b) the area that was subsequently used to evaluate the deformation field.

aggregates relative to the pore network would advance our understanding of soil structure. Such approaches would enable investigations on relationships between local and global cohesion. They would also permit a critical scrutiny of aggregate hierarchy theories, as for example presented by Elliott and Coleman (1988) or Six et al. (2004) who suggest that aggregates of different sizes are confined by pores with corresponding diameters, but are criticized that convincing scientific evidence for this claim is still missing.

Preserving the information on the original location of aggregates requires delineating them in undisturbed soil. Here, non-invasive

imaging methods are potentially useful, first and foremost 3-D X-ray tomography, which visualizes local material densities. If aggregates are delimited by inter-aggregate pores, the latter should be visible in X-ray images, provided the pores are larger than the image resolution. Such an approach works reasonably well for recently tilled soil. Aggregates are easily outlined by visual inspection in X-ray images of topsoil samples ( $\phi \approx 60\text{--}100\text{ mm}$ ) from conventionally ploughed agricultural fields (Jarvis et al., 2017; Schlüter et al., 2018). The same two references illustrate that this is no longer possible for soil layers below the tillage depth or untilled soil in general. In the latter cases, the soil matrix does not present itself as an ensemble of aggregates, but fused and welded together to a homogeneous mass. At a smaller scale ( $\phi \approx 1\text{--}10\text{ mm}$ ) a similar observation can be made (Winstone et al., 2019; Yu et al., 2018). Empirical evidence suggest that such observations are rather the rule than the exception and have led Young et al. (2001) to the statement that inter-aggregate pores do not exist in soil that has not been subject to mechanical forces like they are exerted under tillage operations. Given such evidence, Baveye (2020) claimed that it is “in general impossible to identify aggregates in 3-D (X-ray) CT images of soil samples”.

In this study, we investigated this claim under the assumption that aggregates are delimited by planes of weakness rather than pores, which would require a force to activate the planes of weakness to create cracks to be able to delineate aggregates. We focused on soil samples of several centimetre diameter and exploited tensile forces that occur in drying soils with sufficient amounts of shrinking and swelling clay minerals. The shrinking regions in drying soil are necessarily confined by expanding regions, where either cracks develop or the soil matrix is stretched. We then interpreted the expanding regions as planes of weakness that we used to identify soil aggregates in time-lapse X-ray images, using correlative imaging. We moreover tested and expanded an alternative approach to delineate aggregates in X-ray images that was recently proposed by Yudina and Kuzyakov (2019). We then evaluated whether the X-ray image derived aggregates had comparable properties to aggregates that were physically created from the same soil samples in drop shatter tests. To examine how pore networks influence the fragmentation of the soil we also investigated correlations between measures of soil aggregate sizes and morphological properties of the pore network of the respective intact soil samples.

## 2. Material and methods

### 2.1. Soil sampling and site properties

Eight soil samples, two from each of four different sampling locations, were taken on the 9th of August 2017 near Uppsala, Sweden. The soils cover a wide range of clay contents. At Nântuna (NA), the topsoil texture corresponds to a sandy loam. At the time of sampling, the field was under ley, with couch grass (*Elymus repens*) growing in abundance. The soil texture at the site close to Hammarbyallén (HA) in Ultuna is sandy clay loam. It was cropped with a poorly developed clover (*Trifolium*) ley. The sampling location near Krusenberg (KB) was under a grass ley. The soil texture is clay loam. The fourth site (RA), which is located about 20 m from the long-term fertilization experiment RAM 1956 in Ultuna features soil with a clay loam to clay texture (e.g. Kirchmann and Gerzabek, 1999). The site was cropped with wheat (*Triticum*) at the time of sampling. More details on the soil properties of each site are listed in Table 1.

Prior to sampling, the top 30 to 100 mm of soil, which had a large abundance of roots, were removed to facilitate sampling. We then obtained the samples by gently pushing hollow aluminium cylinders (67 mm inner diameter, 60 mm height) into the ground with the aid of a drop hammer, whereupon they were excavated carefully. Note that the columns were not filled to the rim but instead ranged between heights of 48 to 58 mm.

We calculated bulk densities from the weights of oven-dry (105 °C) soil and volumes of the samples derived from X-ray images. Total

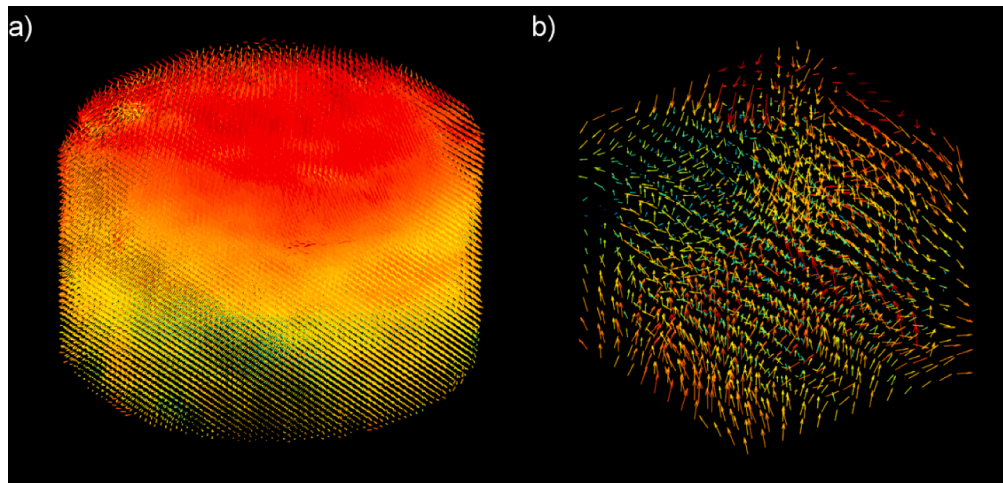


**Fig. 3.** (a) The vector field quantifying the volume displacements between a tension of 50 cm and the oven-dry state for the sample shown in Fig. 2. In (b), the displacement vectors in a cube of 14.4 mm edge-length from the same sample is shown. The colours are related to the magnitude of the displacement vectors. Hot colours indicate large, cold colours small local displacements.

porosities were estimated assuming a mineral density of  $2.65 \text{ g cm}^{-3}$  and a soil organic matter density of  $1.4 \text{ g cm}^{-3}$ , using a factor of two to convert soil organic carbon to soil organic matter (Pribyl, 2010).

## 2.2. Water retention measurement

Where necessary, holes at the bottom of the soil samples were filled with fine sand to provide a good hydraulic contact during the following water retention measurements. Then, a polyamide cloth (mesh size 50  $\mu\text{m}$ ) was applied to the column bottoms to avoid loss of soil. The soils were slowly saturated from the bottom. The samples were placed on a sandbed, where they were drained to a tension of 1 cm, relative to the lower surface of the soil columns. When the columns had reached hydraulic equilibrium, they were weighed and scanned using the X-ray scanner at the Department of Soil and Environment at the Swedish University of Agricultural Sciences (SLU). The samples were then again placed on the sand bed for equilibration to the next tension step. In this way, weights and 3-D X-ray images at the tensions of 15, 50 and 100 cm were obtained, all relative to the bottom surface of the column. Two additional tension steps, namely at 300 and 600 cm were measured in suction pots in which kaolin clay was used to ensure a good hydraulic contact to the soil. Finally, the samples were oven-dried at 105 °C, weighed and 3-D X-ray images were recorded one last time. In this study, we evaluated only the images taken at a matric tension of 50 cm and after oven drying.

We carried out drop-shatter tests following Marshall and Quirk (1950). After oven drying, the intact soil could easily be removed from the cylinders. The soil samples were then dropped from a height of 2 m on a steel tray placed on a concrete floor. We collected and sieved the soil fragments created upon the impact, in the following referred to as aggregates. The largest fragments were weighed. If the weight of a fragment was larger than an arbitrarily chosen threshold of 15 g, we dropped the fragment once more from the same height. We repeated this procedure until all fragments were below the weight threshold. We dry-sieved the aggregates using mesh-sizes of 32, 16, 8, 4 and 2 mm, using a stack of sieves. We shook the sieve-stack 10 times by hand. We then used a brush to gently move the aggregates on each sieve around to make sure that only aggregates with diameters larger than the mesh size were retained. We calculated an aggregate size distribution ( $\text{ASD}_s$  (g), where the subscript  $s$  stands for 'shattered') assuming that the aggregate bulk density  $\rho_a$  ( $\text{g cm}^{-3}$ ) was constant for all fractions. The aggregate bulk density  $\rho_a$  was estimated from the weight of the oven-dry sample divided by the bulk soil volume minus the volume of the pores that had drained at a tension of 1 cm. The effective aggregate diameter  $d_i$  (cm) for each

sieved fraction  $i$  was calculated as the geometric mean of the two respective mesh sizes, i.e. 1.4, 2.8, 5.7, 11.3 and 22.6 (Hadas and Wolf, 1983). The mean aggregate diameter,  $d$  (mm), was obtained as the weight-weighted geometric mean of the effective diameters.

## 2.3. X-ray imaging

The X-ray scanner used in this study was a GE v|tome|x 240 X-ray scanner with a tungsten target and a 16" flat panel detector with a four-megapixel resolution (GE DRX250RT). The columns were imaged at tube voltages of 160 kV and a current of 500  $\mu\text{A}$ . A 2.2 mm thick copper filter was used to remove low-frequency X-rays from the beam to reduce beam-hardening artefacts. The exposure time per radiograph was 133 ms. We used  $2 \times 2$  binning, i.e. each four neighbouring detector crystals were averaged for each individual radiograph pixel. The edge length of each image voxel was 0.12 mm, which corresponds to a feature detection size of approximately 0.24 mm. We referred to the imaged pores as macropores in the following. A total of 2000 radiographs were acquired per 3-D image. The 3-D images were reconstructed using the GE software datos|x 2.1.0 RTM.

## 2.4. Image processing

We used the ImageJ/Fiji (Schindelin et al., 2012; Schneider et al., 2012) plugin SoilJ (Koestel, 2018) to detect the aluminium column outlines automatically. SoilJ was then used to rotate the columns into an upright position and to move them to the centre of the image canvas. Voxel layers above and below the upper and lower ends of the soil columns were removed. The grey-scale of all collected X-ray images was calibrated to the 0.1 percentile of the grey-values inside the soil volume and the grey value of the aluminium column wall, assigning these two imaged phases to grey-values of 5,000 and 20,000, respectively. Then a 3-D median filter with a radius of two voxels was applied, followed by an unsharp-mask with a standard deviation of two voxels and a weight of 0.6. Finally, we manually aligned the images of the wet (50 cm tension) and oven-dry states of each individual sample as well as possible.

## 2.5. Quantification of volume deformation

We used a particle tracking approach similar to the one outlined by Schlüter et al. (2016), who tracked the location of mineral grains in time-lapse X-ray images. Due to a lack of easily segmentable mineral grains in some of the samples, we applied the particle tracking directly on features in the unsegmented images. In short, the two images of each

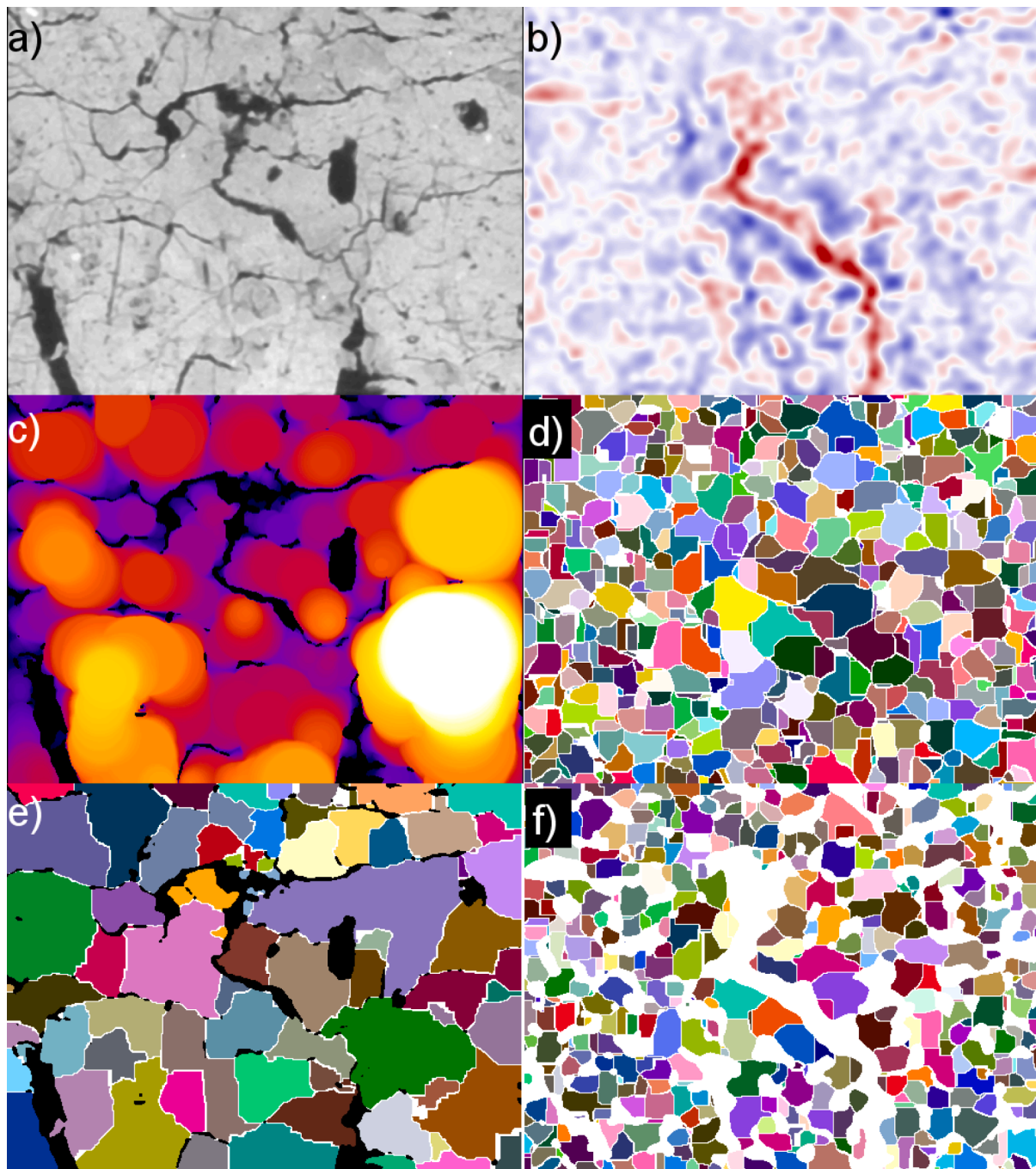


**Fig. 4.** (a) a vertical cross section of the X-ray image of sample KB1; (b) the respective local volume deformation field,  $dV/V_0$ , where blue colours depict shrinking and red colours expanding regions; (c) aggregate sizes  $D_{Y0}$  as quantified based on the approach in (Yudina and Kuzyakov, 2019); (d) aggregate outlines  $D_{D0}$  using the entire local volume deformation field; (e) aggregate outlines  $D_{Y+}$  derived using the extension of the YK-method; (f) aggregate outlines  $D_D$  using only local shrinking volumes.

individual soil sample were first cut to the same canvas size. Then the image taken at 50 cm tension was automatically aligned to the image of the oven-dry state, which served as a reference. The alignment was carried out with the Elastix software (Klein et al., 2010; Shamonin et al., 2014) using a rigid transformation. In the next step, the features in the oven-dry image were mapped to the ones in the respective sample at a tension of 50 cm. We achieved this using the B-spline transform implemented in Elastix. The underlying algorithm aims at minimizing the Mattes' mutual information criterion (Mattes et al., 2001) between voxels of the two overlaid images. As a regularization, a smoothness penalty ('bending energy', Klein et al., 2010) was introduced into the

respective objective function. The weight of the penalty term was determined visually by trial and error for a few example images. Based on these trials, the penalty weight was set to a constant value of 20 for all eight image-registrations that we performed in this study, enabling a quantitative comparison of the registration results. Convergence was enabled and accelerated by running the registration first for a strongly reduced spatial resolution, which was iteratively increased when the objective function had converged. We carried out this so-called pyramid schedule with resolution reductions by factors of 32, 16, 8, 4 and 2, respectively.

The result of the B-Spline registration is a 3-D field of the displace-

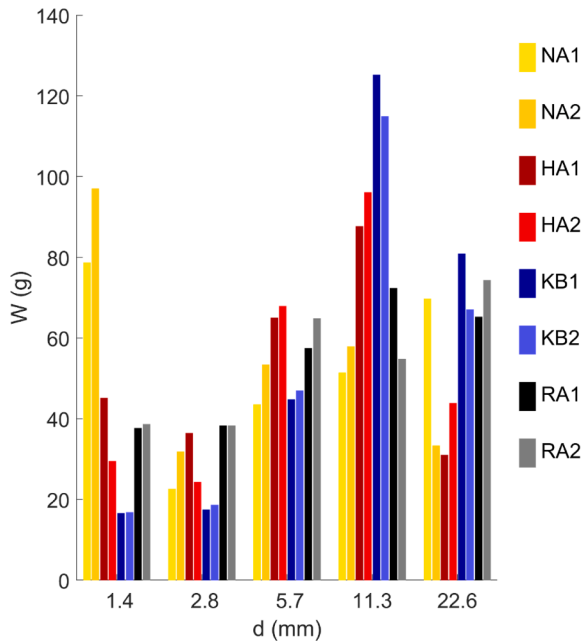


Fig. 5. Results of the drop shatter tests where  $d$  is the geometric mean aggregate diameter and  $W$  the weight fraction after correction for differences in the sample volumes.

ment vectors  $\mathbf{x}$  (mm). These were then used to calculate deformation gradient tensors

$$\mathbf{F} = \nabla \mathbf{x} + \mathbf{I} \quad (1)$$

for each image voxel, where  $\nabla$  denotes the gradient and  $\mathbf{I}$  is the identity matrix.

From the deformation gradient tensor, the local change in volume relative to the original volume was calculated for each image voxel by

$$dV/V_0 = \det \mathbf{F} - 1 \quad (2)$$

which is expressed in percent in the following.

## 2.6. Image analyses

### 2.6.1. Image segmentation

The images were binarized into air-filled pores and non-pores (i.e. particulate organic matter, soil matrix and sand and gravel) using an operationally defined joint threshold for all 16 investigated grey-scale calibrated X-ray images. Upon visual inspection of some of the images the threshold was set to 11,000, a grey-value clearly larger than the location of the minimum (app. 8500) between air and matrix peaks in the joint histogram. In this way, more of the small pores and cracks, were visible in the segmented image.

### 2.6.2. Selection of region of interest

We aimed at selecting a region of interest (ROI) that excluded larger registration artefacts that were located close to the sample walls as well as close to the top and bottom sample surfaces (see below). To do so, we removed approximately 8 and 3 mm from the top and bottom surface of the soil volumes, respectively, and the 3 mm next to the column walls when analyzing both the segmented images and the image with the local volume changes  $dV/V_0$  (see equation (2)). The resulting ROI had a diameter of 59.5 mm and varied in heights between 37.7 and 47.1 mm, depending on the height of the soil sample.

## 2.7. Approaches to identify aggregates in X-ray images

### 2.7.1. Yudina and Kuzyakov's method

Yudina and Kuzyakov (2019) used the maximum inscribed sphere method (Hildebrand and Rügsegger, 1997) to illustrate that aggregates may be present within the soil matrix. We will refer to this method as YK-method in the following. The YK-method simply applies the maximum inscribed sphere method on the soil matrix phase of binary images and, hence, provides a local measure of its diameter. In other words, the YK-method identifies and quantifies the diameter of soil matrix regions that are devoid of image-resolvable pores. At the same time, it obviously quantifies the average distance between imaged pores. The results for the YK-method depend on how the image processing steps are carried out to achieve the binary image of the soil matrix, especially on choice of segmentation method. We did not investigate impacts of different potentially viable segmentation approaches due to their large number. The general impact of the segmentation on results extracted from image data has been already investigated in several publications (e.g. Baveye et al., 1998; Baveye et al., 2010). We simply used the inverse of the binary image of the imaged pore space, i.e. the non-pore phase (see above) as our image of the soil matrix. The segmented matrix also included particulate organic matter as well as gravel and sand grains, as an ensemble of physically created aggregates would.

In shrinking and swelling soils, the results of the YK-method also depend on the soil water content as more and more cracks become visible in the X-ray images upon drying. We therefore applied the YK-method on the X-ray images taken after oven drying as this image features most visible cracks and should, therefore, provide the clearest delineations of aggregate boundaries following the method of Yudina and Kuzyakov (2019). This approach is also most reasonable as the soil samples were drop-shattered after oven drying.

Geometric mean aggregate diameter,  $D_{Y0}$  (mm) and aggregate size distribution  $ASD_{Y0}$  were directly obtained from the histogram of the maximum inscribable spheres image. We did not calculate aggregate surface areas because the aggregate boundaries are not defined by the method. For the sake of simplicity, we used the mean aggregate diameters as a proxy for all image-derived soil aggregate sizes.

The original YK-method does not provide discrete aggregates and a comparison with fragments obtained from the drop shatter test is difficult. Rather than an aggregate size,  $D_{Y0}$  is the average distance between imaged pores. We therefore modified the approach and ran a 3-D distance transform watershed algorithm on the binary images using local distance maxima as seeds/sources, which yielded aggregates with distinct boundaries. Here we chose the 'Borgefors (3,4,5)' algorithm (Borgefors, 1986) implemented in the ImageJ plugin MorphoLibJ (Legland et al., 2016) with 26 nearest neighbors. The algorithm takes local maxima of the distance transform image as seed points. The parameter that sets a threshold to the "topographic" prominence of the chosen maxima was set to its default value in MorphoLibJ. The statistics of the delineated aggregates and their size distribution were then extracted using the labelled component analyzer of MorphoLibJ as implemented into SoilJ. We calculated mean effective aggregate diameters, approximating the aggregates as spheres with equivalent volumes. We refer to the resulting geometric mean aggregate diameter and size distribution by  $D_{Y+}$  (mm) and  $ASD_{Y+}$ , respectively.

### 2.7.2. Deformation gradient tensor based method

The local volume changes between a tension of 50 cm and the oven-dry state,  $dV/V_0$ , can be used to divide the imaged soil volume into shrinking (negative  $dV/V_0$ ) and swelling regions (positive  $dV/V_0$ ). We exploited this by applying the classical watershed algorithm (Soille and Vincent, 1990) implemented in MorphoLibJ with 26 nearest neighbors to the deformation image. Here we used local shrinkage minima as seed regions. The crests through the expanding regions defined aggregate boundaries, i.e. planes of weakness. The statistics of the delineated

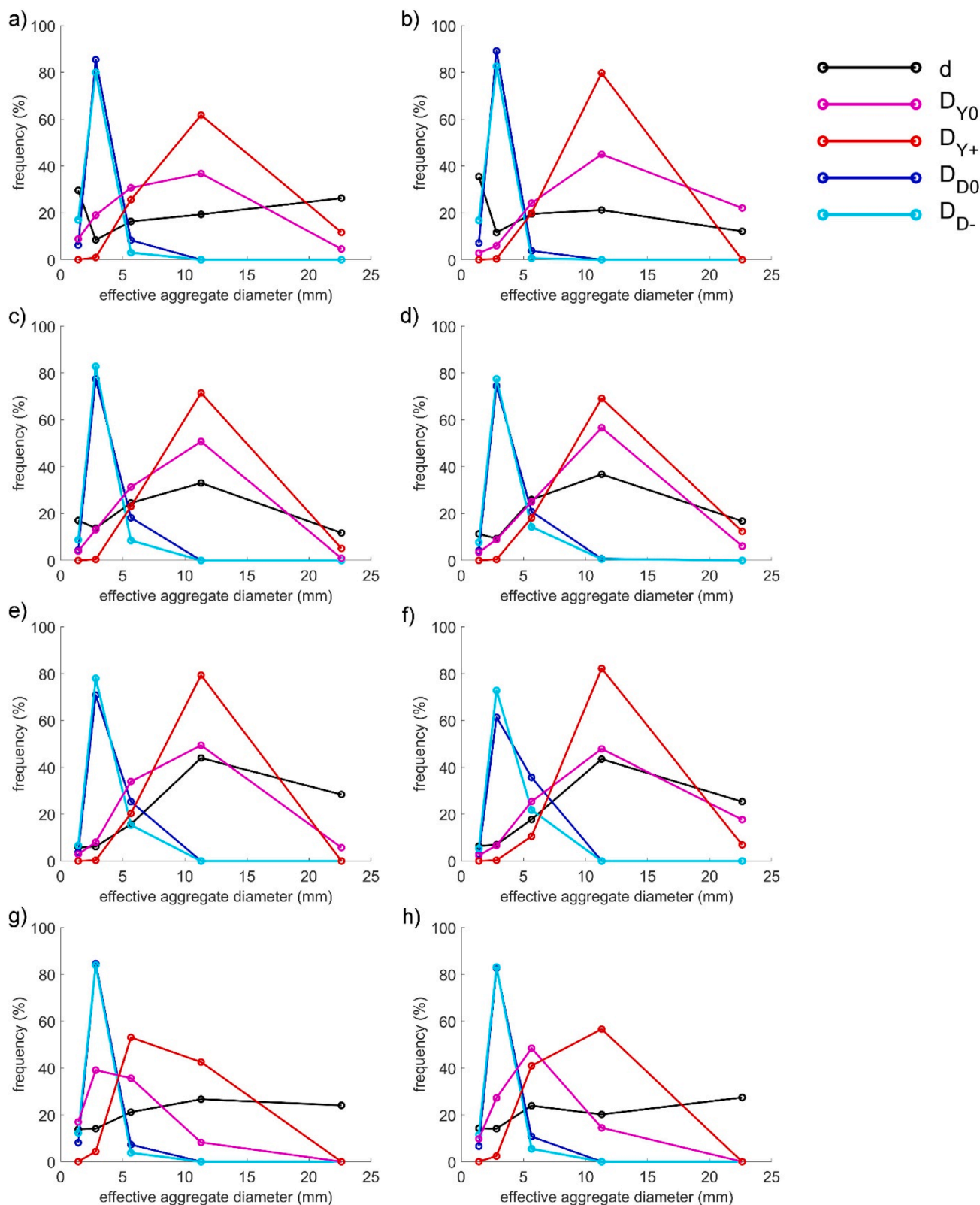


**Fig. 6.** Comparison of the size distribution of the image and the drop-shatter derived aggregates from the soils sampled at Nântuna (a & b, i.e. NA1 & NA2), Hammarbyallén (c & d; i.e. HA1 & HA2), Krusenberget (e & f, i.e. KB1 & KB2) and RAM 1956 (g & h, i.e. RA1 & RA2).

aggregates and their size distribution were extracted as described above for the modified YK-method. The geometric mean effective aggregate diameters and size distribution are referred to as  $D_{D0}$  (mm) and  $ASD_{D0}$ .

With the above method, the aggregates will occupy the whole

volume while in reality the soil contains pores. This should lead to an overestimation of aggregate sizes. We therefore also investigated deriving aggregates from only regions with negative  $dV/V_0$ , i.e. shrinking regions. Here, we first excluded all voxels with zero or positive

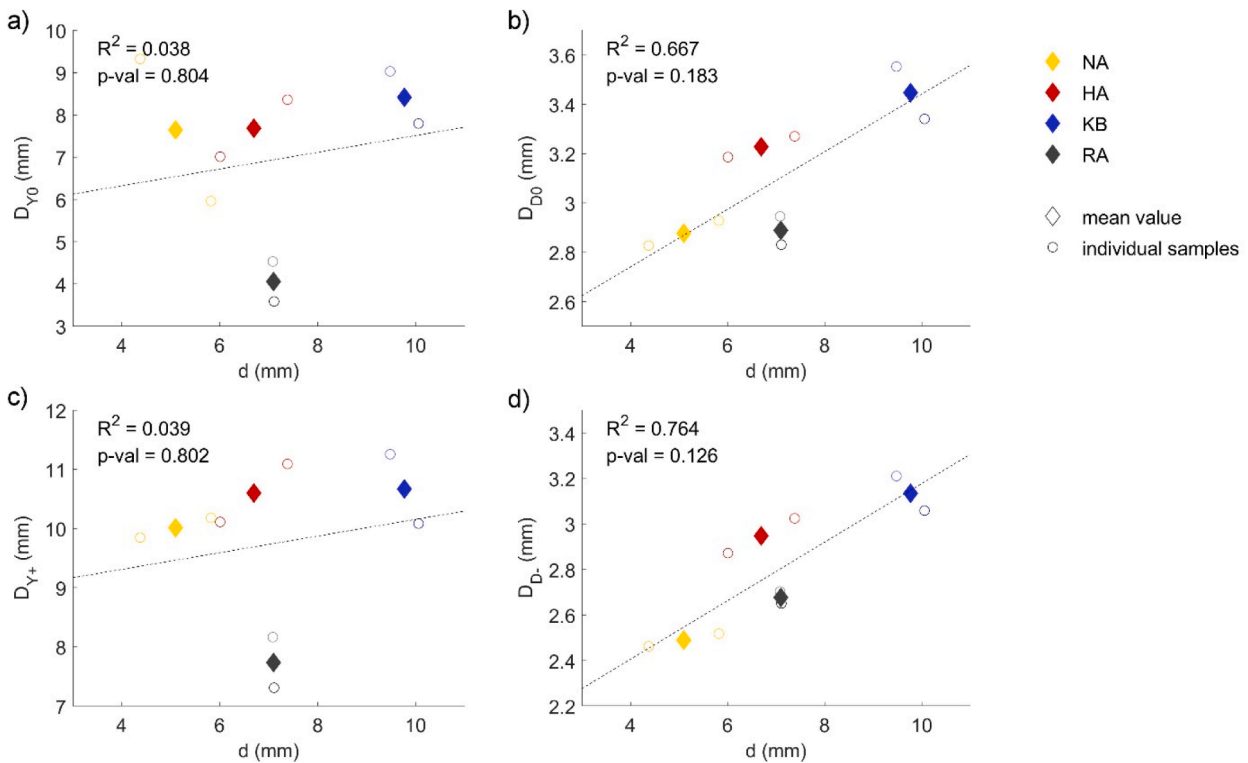


Fig. 7. Regressions between image and drop-shatter derived mean aggregate diameters. The statistics correspond to the mean values.

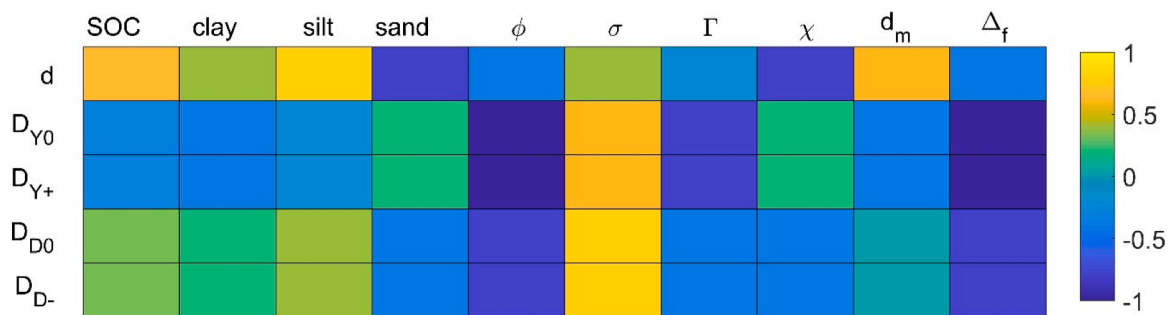


Fig. 8. Spearman correlation coefficients between geometric mean aggregate diameters and some pore-network morphology measures. Here,  $d$  stands for the diameter of the aggregates from the drop-shatter tests;  $D_{Y0}$  for the diameters quantified based on the YK-approach as outlined in Yudina and Kuzyakov (2019);  $D_{Y+}$  aggregate diameters using the extension of the YK-method;  $D_{D0}$  aggregate diameters using the entire local volume deformation field;  $D_{D-}$  aggregate diameters using only local shrinking volumes. Moreover, SOC stands for soil organic carbon, ‘clay’, ‘silt’, ‘sand’ denote the clay, silt and sand content, respectively,  $\phi$  the imaged porosity,  $\sigma$  the imaged pore surface area,  $\Gamma$  the  $\Gamma$ -connectivity,  $\chi$  the Euler-Poincaré number,  $d_m$  the mean imaged pore diameter and  $\Delta_f$  the fractal dimension. Asterisks indicate significant correlations (p-value of 0.05).

$dV/V_0$ . Then we ran the classical watershed algorithm on the remaining parts of the image. The image statistics were derived as above and diameter and aggregate size distribution are denoted as  $D_{D-}$  (mm) and  $ASD_{D-}$ .

It is self-evident that also the deformation gradient tensor based methods are dependent on the image processing steps used to calculate them. Most prominently, the regularization parameter chosen in the B-spline registration as well as the selection of seed regions for the watershed algorithms will influence the results. We did not investigate effects of specific image processing steps on resulting  $D_{D0}$  and  $D_{D-}$  due to the large workload that is associated with such a task. The workflow in Fig. 1 summarizes the processing steps that were needed to delineate the aggregates within the X-ray images.

### 2.7.3. Analyses of pore-network morphologies

We used SoilJ, which in turn uses the Bonej (Doube et al., 2010) and the MorphoLibJ plugins, to calculate several morphological properties of the imaged soil pore network. Apart from the macroporosity  $\phi$  ( $\text{mm}^3 \text{mm}^{-3}$ ), and the specific macropore surface area,  $\sigma$  ( $\text{mm}^2 \text{mm}^{-3}$ ), we calculated the fractal dimension,  $\Delta_f$ , and two connectivity measures: the Euler-Poincaré characteristic  $\chi$  (-) and the  $\Gamma$ -connectivity (-), where the latter is defined as

$$\Gamma = \frac{\sum_{i=1}^N n_i^2}{(\sum_{i=1}^N n_i)^2} \quad (3)$$

where  $n_i$  is the number of pore voxels contained in pore cluster  $i$  and  $N$  is the total number of pore clusters. We also quantified the average macropore diameter,  $d_m$  (mm), using the maximum inscribed sphere

method. All statistical analyses in this study were carried out with Matlab (version 9.5).

### 3. Results and discussion

#### 3.1. Quality of image registrations

The application of the B-spline registration approach is illustrated in Fig. 2, using data from the Krusenberg 1 sample, (a) at a tension of 50 cm and (b) at the oven dry state. The second image has been registered to the first one. The composite image shown in Fig. 2c depicts the extent to which the registration recovered the soil volume deformations. White and gray colours indicate a successful match of soil structural features after the registration. Red and blue colours indicate either a) a change in local density in between the two images or, when appearing in pairs, b) a mismatch of features, i.e. registration errors. It is clear that strong mismatches in patterns appeared outside the ROI that was considered for registration. For example, the strongly deformed right-hand aluminium wall of the soil sample simply resulted from the fact that the registration was not constrained by data. However, from Fig. 2c it is obvious that there were also several registration errors present inside the ROI, mainly in regions close to the column walls. In future studies, the column wall should therefore be included into the registration process to better constrain the registration for soil regions close to the wall. Another region with registration errors is located close to the top surface of the soil sample. In the central portions of the soil sample, the registration worked reasonably well, despite many larger cracks that are depicted in red in Fig. 2c. Here the soil structural features have been matched correctly and the green colour indicates the loss of density at the respective locations, where cracks had opened during drying. Note that the reddish hue of the soil matrix corresponds to local density differences between the soil sample at matrix potential  $-50$  cm and the oven-dried state, caused by loss of water.

#### 3.2. Patterns in deformation fields

Fig. 3a and b show a displacement vector-field obtained from the B-spline registration. Since the soil was constrained at the bottom and at the cylinder walls, the largest displacements took place close to the soil surface (Fig. 3a). Local variations in displacement were apparent in both the vertical and horizontal directions (Fig. 3b). Fig. 4a shows a vertical cross-section of the X-ray image of the Krusenberg 1 sample at the oven-dry state alongside deformation data  $dV/V_0$  (Fig. 4b). The deformation patterns were generally not correlated with the distance to the cylinder walls or with the vertical position in the sample. Regions with large deformations (i.e. both shrinkage and expansion) were commonly found in the vicinity to large, drying-induced cracks. However, many of the moderately expanding regions were located in soil matrix regions devoid of visible cracks. In such cases, the matrix may be in general unstable and disintegrate into smaller fragments upon drop-shattering. Fig. 4a and b also show that not all pores were associated with large deformations, which indicates that these pores did not correspond to planes of weakness.

#### 3.3. Image derived soil aggregates

Fig. 4c shows the local thicknesses of the soil matrix, which were used in Yudina's original method. The figure illustrates the absence of clearly defined aggregate boundaries. Results from the extended version of the YK-method that introduces clear aggregate boundaries is shown in Fig. 4e.

Fig. 4d and f show delineated aggregates for the deformation gradient tensor based methods. The most striking difference to the image-derived aggregates based on the YK-method (Fig. 4c and e) was the much smaller diameters for the deformation gradient tensor field derived aggregates.

#### 3.4. Drop-shatter tests

The two samples taken from the same site generally had similar aggregate size distributions created in the drop shatter tests (Fig. 5). The large deviation between the two samples from Nântuna (NA 1 and 2) for the largest aggregate fraction may be related to the activities of an earthworm that was trapped in one of the samples. The earthworm casts and excretions may have increased the cohesion between the soil particles and led to larger aggregates. The earthworm cast may also be responsible for the higher soil organic carbon content (SOC) in this sample. The samples from Nântuna showed a bi-modal aggregate size distribution with average diameter maxima of 1.4 and 11.3 mm. Particles in the finest sieved fraction possibly corresponded to individual sand grains since the sand content was large (Table 1). The Krusenberg (KB) samples showed a pronounced unimodal aggregate size distribution with a maximum at 11.3 mm diameter. The size distribution for the samples from Hammarbyallén (HA) was intermediate to the ones from Nântuna and Krusenberg. The soil taken from next to the Ramförsök (RA) had the most evenly distributed aggregate sizes, while larger diameters slightly dominated smaller ones.

#### 3.5. Comparison between image and drop-shatter derived aggregates

The match between the aggregate size distributions from the YK-methods and the drop-shatter test were better than the match between the distributions from the deformation gradient tensor method and the drop shatter tests (Fig. 6). Here, Yudina and Kuzyakov's original method yielded better results than the extended one. However, while excellent or at least acceptable matches between  $ASD_{V0}$  and  $ASD_s$  were observed for the samples from Hammarbyallé (Fig. 6c and d) and Krusenberg (Fig. 6e and f), the matches were poor for the samples from Nântuna (Fig. 6a and b) and the Ramförsök (Fig. 6g and h). Excellent matches between image and drop-shatter derived aggregate size distributions do not necessarily mean that individual aggregates were correctly matched. Nevertheless, it encourages further investigations. In contrast, the aggregates derived from the deformation gradient tensor did not at all match the size distribution observed in the drop-shatter tests (Fig. 6), but exclusively showed unimodal distributions around a diameter of 2.8 mm.

One possible explanation for this discrepancy is that the force applied during the drop shatter test was not strong nor homogenous enough to break the soil at all planes of weakness indicated by the expanding regions. Another possible explanation is that the expanding regions do not correspond to the planes of weakness where the soil broke upon shattering. Here, also imperfections of the elastic image registration need to be considered. Finally, it could be argued that the choice of using all centres of locally shrinking regions led to an overestimation of the number of individual aggregates and, hence, an underestimation of aggregate sizes. As already discussed, we abstained from fine-tuning approaches for delineating aggregates from the X-ray images due to the large degree of freedom entailed in such an undertaking. Note that tampering with the definitions for seed-regions in the deformation gradient tensor based methods would correspond to trying different segmentation and water-shedding approaches for the YK-based methods. Fine-tuning of the image-based aggregate delineation approaches should be the focus of a follow-up study that involves a clearly larger number of soil samples.

Fig. 7 depicts the relationships between the geometric mean diameters of the image and drop-shatter derived diameters. The regression lines shown in the figures correspond to the mean of each two samples from each site. The intercept was fixed at the origin. While the absolute values of  $D_{D0}$  and  $D_D$  underestimated the results from the drop-shatter tests, both showed large coefficients of determination with  $d$ , with  $D_D$  exhibiting the larger one ( $R^2 = 0.764$  versus  $R^2 = 0.667$ ). These correlations have moderately low p-values of 0.126 and 0.183, respectively. Given the very small number of samples, these values justify further

research on larger sample sets to test whether significant linear relationships are common between drop-shatter and image-derived aggregate properties. Fig. 7a and c show that no correlations exist between the diameters from the YK-methods and the drop-shatter tests.

Finally, caveats of the here presented approach need to be discussed that are intimately linked with the cohesive forces used to isolate aggregates. It is possible, that the aggregates delineated in this study are biased towards regions with high concentrations of swelling and shrinking clay minerals. It is unclear if thus activated planes of weakness coincide with the outlines aggregates that are created by different physical methods, e.g. drop-shattering of moist soil samples or a sieving method. This should be investigated in future studies. Follow up studies should also check whether the comparison between image and drop-shatter derived aggregates was biased towards positive results. As we drop-shattered the oven-dried samples, they already contained the shrinkage cracks used for the image derived aggregate identifications. They hence already contained the activated planes of weakness when they were physically shattered. If this led to a relevant bias, may be investigated by comparing drop-shatter results from field-wet and dry soil samples.

### 3.6. Comparison of aggregates with the imaged pore network properties

We used Spearman rank correlation coefficients to compare aggregate properties to the morphology of the imaged macropore network because the measures for pore connectivity are known to be non-normally distributed. None of the X-ray derived macropore morphology measures were significantly correlated to the aggregate diameters after shattering of the soil samples (Fig. 8). However, we found the same trend in the relationship between  $d$  and  $\phi$  as Munkholm et al. (2012) who reported a significant positive correlation between the X-ray derived macroporosity and a measure for the soil friability, which is inversely related to the aggregate diameter from drop-shatter tests. Instead, the strongest correlation between  $d$  and a pore morphological measure was with the Euler-Poincaré characteristics  $\chi$  (Fig. 8). It stands out that the Spearman correlation coefficients were identical for both YK-based and both deformation gradient tensor based methods. Negative correlations of all aggregate delineation methods were observed between aggregate diameters and visible porosity  $\phi$ ,  $\Gamma$ -connectivity and fractal dimension  $\Delta_f$ . Such correlations are to be expected as all three parameters indicate larger and more interconnected pore-networks, which means a partitioning of the soil into smaller compartments and therefore, by trend, smaller aggregate diameters.

## 4. Conclusion

In this study, we presented and evaluated methods that enable a delineation of 3-D subunits in X-ray images of undisturbed soil. Similar to traditional methods used to isolate aggregates (e.g. wet-sieving or drop-shatter tests) some of the methods require the application of a force to allow for the identification of aggregates. Comparisons between image and drop-shatter test derived aggregate properties remained inconclusive, regardless of the method. In part, this may be related to the very small number of samples used in our study. Moreover, differences in the result must also be due to the differences in nature of the forces applied, i.e. cohesive forces exerted by soil water under drying and the impact forces in the drop-shatter tests. Nevertheless, we also observed trends in the result that encourage further investigations on larger sample sets as approaches like the ones presented here offer potential to harmonize the two opposing viewpoints on soil structure: the pore phase and the solid phase perspectives.

There is a plethora of image processing choices to be made until aggregates can be delineated in X-ray images. This makes the result of the image-derived aggregate delineation similarly dependent on the chosen method as physically isolated aggregates. Follow up studies need to investigate the sensitivity of the image-derived aggregate outlines to

the chosen field-of-view and the image resolution and to specific choices in the image processing steps, such as different segmentation and registration approaches and respective parameterization. They should also compare image-derived aggregate outlines with results of alternative aggregate isolation methods, notably wet and dry sieving, which are applied more frequently than drop-shatter tests. This would entail X-ray imaging at a smaller scale than the one of the present study, namely a field of view of a few millimeters. At this scale, slaking may be used to break up macroaggregates into microaggregates. If successful, such an approach could be applied to compare aggregate topologies in soils under different land use and management and from different climates, contributing to further elucidate the nature of aggregates and their role in soils.

## Declaration of Competing Interest

The authors declare that they have no known competing financial interests or personal relationships that could have appeared to influence the work reported in this paper.

## Acknowledgements

This project was supported by Stiftelsen Akademiens Kulturtekniska Fond and Stiftelsen Carl-Fredrik von Horns fond that are managed under the umbrella of Kungliga Skogs- och Lantbruksakademien (KSLA) in form of project GFS2019-0144. Moreover, we are thanking Alice Johannes and Thomas Keller for discussions on aggregates and soil shrinkage and for their feedback to an earlier version of this manuscript.

## References

- Baveye, P., Boast, C.W., Ogawa, S., Parlange, J.-Y., Steenhuis, T., 1998. Influence of image resolution and thresholding on the apparent mass fractal characteristics of preferential flow patterns in field soils. *Water Resour. Res.* 34 (11), 2783–2796.
- Baveye, P.C., 2020. Bypass and hyperbole in soil research: Worrysome practices critically reviewed through examples. *Eur. J. Soil Sci.* 72 (1), 1–20.
- Baveye, P.C., Laba, M., Otten, W., Bouckaert, L., Dello Sterpaio, P., Goswami, R.R., Grinev, D., Houston, A., Hu, Y., Liu, J., Mooney, S., Pajor, R., Sleutel, S., Tarquis, A., Wang, W., Wei, Q., Sezgin, M., 2010. Observer-dependent variability of the thresholding step in the quantitative analysis of soil images and X-ray microtomography data. *Geoderma* 157 (1–2), 51–63.
- Borgefors, G., 1986. Distance transformations in digital images. *Computer Vision, Graphics, & Image Processing* 34 (3), 344–371.
- Denef, K., Six, J., Merckx, R., Paustian, K., 2002. Short-term effects of biological and physical forces on aggregate formation in soils with different clay mineralogy. *Plant Soil* 246 (2), 185–200.
- Doube, M., Klosowski, M.M., Arganda-Carreras, I., Cordelières, F.P., Dougherty, R.P., Jackson, J.S., Schmid, B., Hutchinson, J.R., Shefelbine, S.J., 2010. BoneJ Free and extensible bone image analysis in ImageJ. *Bone* 47 (6), 1076–1079.
- Elliott, E.T., Coleman, D.C., 1988. Let the soil work for us. *Ecological Bulletins - Swedish Natural Science Research Council* 39, 23–32.
- Hadas, A., Wolf, D., 1983. Energy efficiency in tilling dry clod-forming soils. *Soil Tillage Res.* 3 (1), 47–59.
- Hildebrand, T., Rügsegger, P., 1997. A new method for the model-independent assessment of thickness in three-dimensional images. *J. Microsc.* 185 (1), 67–75.
- Horn, R., Taubner, H., Wuttke, M., Baumgartl, T., 1994. Soil physical properties related to soil structure. *Soil Tillage Res.* 30 (2–4), 187–216.
- Jarvis, N., Larsbo, M., Koestel, J., 2017. Connectivity and percolation of structural pore networks in a cultivated silt loam soil quantified by X-ray tomography. *Geoderma* 287, 71–79.
- Kirchmann, H., Gerzabek, M.H., 1999. Relationship between soil organic matter and micropores in a long-term experiment at Ultuna, Sweden. *J. Plant Nutr. Soil Sci.* 162 (5), 493–498.
- Klein, S., Staring, M., Murphy, K., Viergever, M.A., Plum, J., 2010. Elastix: A Toolbox for Intensity-Based Medical Image Registration. *IEEE Trans. Med. Imaging* 29 (1), 196–205.
- Koestel, J., 2018. SoilJ: An ImageJ Plugin for the Semiautomatic Processing of Three-Dimensional X-ray Images of Soils. *Vadose Zone J.* 17 (1), 170062. <https://doi.org/10.2136/vzj2017.03.0062>.
- Kravchenko, A., Otten, W., Garnier, P., Pot, V., Baveye, P.C., 2019. Soil aggregates as biogeochemical reactors: Not a way forward in the research on soil-atmosphere exchange of greenhouse gases. *Glob. Change Biol.* 25 (7), 2205–2208.
- Legland, D., Arganda-Carreras, I., Andrey, P., 2016. MorphoLibJ: integrated library and plugins for mathematical morphology with ImageJ. *Bioinformatics* 32 (22), 3532–3534.
- Letey, J., 1991. The study of soil structure: Science or art. *Aust. J. Soil Res.* 29 (6), 699–707.

- Marshall, T., Quirk, J., 1950. Stability of structural aggregates of dry soil. *Aust. J. Agric. Res.* 1 (3), 266–275.
- Martin, J.P., Martin, W.P., Page, J.B., Raney, W.A., de Ment, J.D., 1955. Soil Aggregation. *Adv. Agron.* 1–37.
- Mattes, D., Haynor, D.R., Vesselle, H., Lewellyn, T.K., Eubank, W., 2001. Nonrigid multimodality image registration, *Medical Imaging 2001*. SPIE, pp. 12.
- Munkholm, L.J., Heck, R.J., Deen, B., 2012. Soil pore characteristics assessed from X-ray micro-CT derived images and correlations to soil friability. *Geoderma* 181/182, 22–29.
- Munkholm, L.J., Heck, R.J., Deen, B., Zidar, T., 2016. Relationship between soil aggregate strength, shape and porosity for soils under different long-term management. *Geoderma* 268, 52–59.
- Pribyl, D.W., 2010. A critical review of the conventional SOC to SOM conversion factor. *Geoderma* 156 (3–4), 75–83.
- Rabot, E., Wiesmeier, M., Schlüter, S., Vogel, H.-J., 2018. Soil structure as an indicator of soil functions: A review. *Geoderma* 314, 122–137.
- Rillig, M.C., Aguilar-Trigueros, C.A., Bergmann, J., Verbruggen, E., Veresoglou, S.D., Lehmann, A., 2015. Plant root and mycorrhizal fungal traits for understanding soil aggregation. *New Phytol.* 205 (4), 1385–1388.
- Schindelin, J., Arganda-Carreras, I., Frise, E., Kaynig, V., Longair, M., Pietzsch, T., Preibisch, S., Rueden, C., Saalfeld, S., Schmid, B., Tinevez, J.-Y., White, D.J., Hartenstein, V., Eliceiri, K., Tomancak, P., Cardona, A., 2012. Fiji: an open-source platform for biological-image analysis. *Nat. Methods* 9 (7), 676–682.
- Schlüter, S., Großmann, C., Diel, J., Wu, G.-M., Tischer, S., Deubel, A., Rücknagel, J., 2018. Long-term effects of conventional and reduced tillage on soil structure, soil ecological and soil hydraulic properties. *Geoderma* 332, 10–19.
- Schlüter, S., Leuther, F., Vogler, S., Vogel, H.J., 2016. X-ray microtomography analysis of soil structure deformation caused by centrifugation. *Solid Earth* 7 (1), 129–140.
- Schneider, C.A., Rasband, W.S., Eliceiri, K.W., 2012. NIH Image to ImageJ: 25 years of image analysis. *Nat. Methods* 9 (7), 671–675.
- Sexstone, A.J., Revsbech, N.P., Parkin, T.B., Tiedje, J.M., 1985. Direct measurement of oxygen profiles and denitrification rates in soil aggregates. *Soil Sci. Soc. Am. J.* 49 (3), 645–651.
- Shamonin, D., Bron, E., Lelieveldt, B., Smits, M., Klein, S., Staring, M., 2014. Fast Parallel Image Registration on CPU and GPU for Diagnostic Classification of Alzheimer's Disease. *Front. Neuroinf.* 7 (50).
- Six, J., Bossuyt, H., Degryze, S., Denef, K., 2004. A history of research on the link between (micro)aggregates, soil biota, and soil organic matter dynamics. *Soil Tillage Res.* 79 (1), 7–31.
- Soille, P., Vincent, L., 1990. Determining watersheds in digital pictures via flooding simulations, *Proceedings of SPIE - The International Society for. Opt. Eng.* 240–250.
- Stoops, G., 2009. Seventy years' "Micropedology" 1938–2008: The past and future. *Journal of Mountain Science* 6 (2), 101–106.
- Tisdall, J.M., Oades, J.M., 1982. Organic-matter and water-stable aggregates in soil. *J. Soil Sci.* 33 (2), 141–163.
- Totsche, K.U., Amelung, W., Gerzabek, M.H., Guggenberger, G., Klump, E., Knief, C., Lehndorff, E., Mikutta, R., Peth, S., Prechtel, A., Ray, N., Kögel-Knabner, I., 2018. Microaggregates in soils. *J. Plant Nutr. Soil Sci.* 181 (1), 104–136.
- Winstone, B.C., Heck, R.J., Munkholm, L.J., Deen, B., 2019. Characterization of soil aggregate structure by virtual erosion of X-ray CT imagery. *Soil Tillage Res.* 185, 70–76.
- Young, I.M., Crawford, J.W., Rappoldt, C., 2001. New methods and models for characterising structural heterogeneity of soil. *Soil Tillage Res.* 61 (1–2), 33–45.
- Yu, X., Peng, G., Lu, S., 2018. Characterizing Aggregate Pore Structure by X-Ray Micro-Computed Tomography and a Network Model. *Soil Sci. Soc. Am. J.* 82 (4), 744–756.
- Yudina, A., Kuzyakov, Y., 2019. Saving the face of soil aggregates. *Glob. Change Biol.* 25 (11), 3574–3577.